

1 Introduction

Techniques to recover object shapes from reflectance and shading information, contained in either a single intensity image or multiple intensity images, are categorized into two main groups. One is called shape from shading, and the other is generally known as photometric stereo. Horn originally introduced the shape from shading technique [4] which recovered object shape from a single intensity image by using the characteristic strip expansion method. Following Horn's method, many other methodologies have been proposed by other researchers. (For instance, the chapter of shape from shading in [2] is a good source of information about the shape from shading techniques.) Woodham [15] proposed a new technique called photometric stereo for shape recovery. This technique uses multiple images with different light source locations. Later, Nayar, Ikeuchi and Kanade [10] developed a technique for recovering object shape and reflectance without any knowledge of surface reflectance.

These techniques for shape recovery have been successfully applied to intensity images taken in a laboratory setup. However, reports of applications for real intensity images of outside scenes have been very limited. Intensity images synthesized or taken in a laboratory setup are well controlled and are less complex than those taken outside under sunlight. For instance, in an outdoor environment, there are multiple light sources of different colors and spatial distributions, namely the sunlight and the skylight. The sunlight can be regarded as yellow point light source whose movement is restricted to the ecliptic¹. On the other hand, the skylight is a blue extended light source which is almost constant over the entire hemisphere. Due to the sun's restricted movement, the problem of surface normal recovery becomes underconstrained under sunlight. For instance, if the photometric stereo method is applied to two intensity images taken outside at different times, two surface normals which are symmetric with respect to the ecliptic are obtained at each surface point. Those two surface normals cannot be distinguished locally because those two surface normal directions give us exactly the same brightness at the surface point.

Another factor that makes reflectance analysis under the solar illumination different is multiple reflection components from the object surface. Reflection from object surfaces may have multiple

1. The great circle of the celestial sphere that is the apparent path of the sun among the stars or of the earth as seen from the sun: the plane of the earth's orbit extended to meet the celestial sphere.

reflection components such as the diffuse reflection component and the specular reflection component. The two reflection components are predicted from the dichromatic reflectance model which was proposed by Shafer [13]. Recently, Sato and Ikeuchi [12] proposed and successfully demonstrated a methodology to separate the two reflection components at each pixel. They used a color image sequence taken with a moving light source. The main advantage of the technique is that it does not require any *a-priori* knowledge of surface reflectance, and only a sequence of observed color vectors at each pixel is necessary.

In other situations, the object may be painted in different colors. In other words, the object has a non-uniform surface albedo. In this case, the traditional techniques for shape recovery cannot be correctly applied because those methods are based on the assumption of a uniform surface albedo. To compensate for this effect, the surface albedo has to be normalized before shape recovery. If the surface albedo varies gradually on the object surface, the normalization can be quite difficult. However, if the problem is limited to special cases where the object surface consists of patches with constant surface albedo, the non-uniform surface albedo can be normalized by using several techniques. Horn [3] used Land's retinex theory [6] to determine surface albedo which is insensitive to an illumination change. By using this technique, the surface albedo can be obtained for each uniform albedo region. Then, the surface albedo can be normalized.

In this paper, we address the three issues involved in analyzing real outdoor intensity images taken under the solar illumination. 1. the multiple reflection components including highlight (the specular reflection component according to the dichromatic reflection model.) 2. the normalization of surface albedo. 3. the unique solution for surface normals under sunlight. For each of these problems, we show a solution and demonstrate the feasibility of the solution by using images which are taken in a laboratory setup and outdoors under the sun.

The paper is organized as follows. The section 2 describes the reflectance model that we used for analyzing outdoor images under solar illumination. The development of the model is based on the dichromatic reflection model and takes into account two light sources of different spectral and spatial distributions. In the section 3, a method to remove the specular reflection component by using a sequence of color images is explained. The normalization of the surface albedo is described in the section 4. A method to obtain two sets of surface normals for the object surface to choose the correct set of surface normals are discussed in the section 5. Experimental results from

a laboratory setup and the outdoor environment will be shown in the section 6 and the section 7, respectively. Concluding remarks are presented in the section 8.

2 Reflection model under solar illumination

2.1 Reflection model with a single light source

In this section, a reflectance model with a single light source is described. We will develop a reflectance model under solar illumination in the section 2.2.

A mechanism of reflection is described in terms of three reflection components, namely the specular spike, the specular lobe, and the diffuse lobe. These reflection components can be represented by the Beckmann-Spizzichino model [1], the Torrance-Sparrow model [14] (or the Beckmann-Spizzino model), and the Lambertian model, respectively [10]. The model of reflection which accounts for all three components tends to be too complicated to be used as a model for actual applications. Thus, a simplified model which represents two reflection components, the specular reflection component and the diffuse reflection component, is used in our analysis. The specular reflection component of the simplified reflection model represents a combination of the specular spike and the specular lobe. The combined specular reflection component is modeled as a simple function such as an impulse function. Nayar called the reflectance model the hybrid reflectance model [10]. In this reflectance model, the pixel intensity of an image is expressed as

$$I = I_D + I_S \quad (\text{EQ1})$$

where I_D is the diffuse reflection component and I_S is the specular reflection component.

In order to simplify the discussion, we develop the reflectance model in a two dimensional planer case instead of the three dimensional case. An equivalent discussion can be applied to the three dimensional case without fundamental differences.

The dichromatic reflection model in the two dimensional planer case can be represented by the bidirectional spectral-reflectance distribution function (BSRDF) as:

$$f_r(\theta_i, \theta_r, \lambda) = c_D(\lambda) g_D(\theta_i, \theta_r) + c_S(\lambda) g_S(\theta_i, \theta_r) \quad (\text{EQ2})$$

where f_r is the BSRDF, $c_D(\lambda)$ and $c_S(\lambda)$ are the spectral reflectance distributions, $g_D(\theta_i, \theta_s)$ and $g_S(\theta_i, \theta_s)$ are the geometrical terms. The subscripts D and S refer to the diffuse reflection component and the specular reflection component, respectively. θ_i and θ_s are the inci-

dent angle and the reflecting angle as shown in Figure 1.

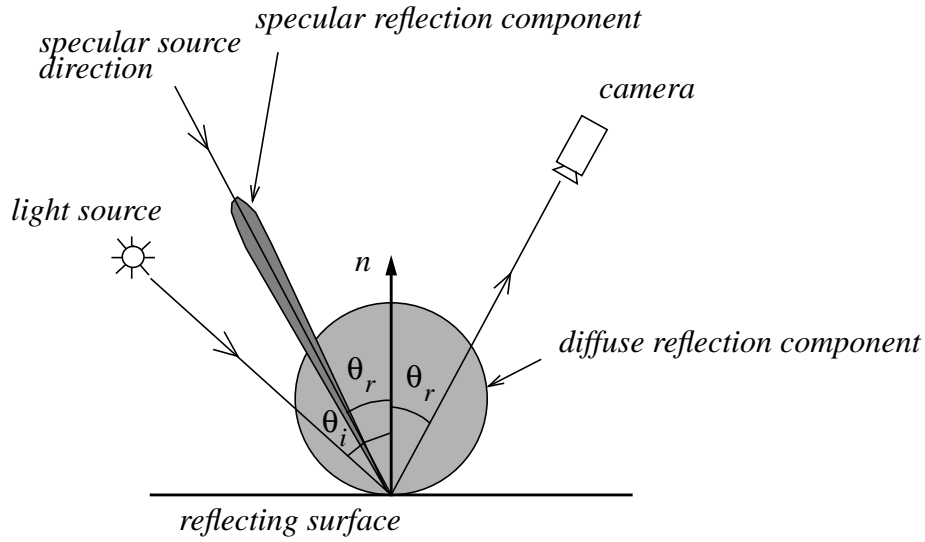


Figure 1 Reflectance model with two reflection components

In most reflectance models, it is assumed that the diffuse reflection component has a spectral distribution different from that of an incident light, while the specular reflection component has a similar spectral distribution. Lee called this model the neutral-interface-reflection (NIR) model [8]. Considering the NIR model, (EQ2) is written as:

$$f_r(\theta_i, \theta_r, \lambda) = c_D(\lambda) g_D(\theta_i, \theta_r) + c_S g_S(\theta_i, \theta_r) \quad (\text{EQ3})$$

Since we assumed that the diffuse reflection component is modeled by the Lambertian model, and the specular reflection component is modeled by a unit impulse function, (EQ3) becomes

$$f_r(\theta_i, \theta_r, \lambda) = c_D(\lambda) \cos\theta_i + c_S \delta(\theta_i - \theta_r) \quad (\text{EQ4})$$

On the other hand, the intensity of incident light onto the object surface (and not into the camera) is represented as:

$$L_i(\theta_i, \lambda) = c(\lambda) L(\theta_i) \quad (\text{EQ5})$$

where $c(\lambda)$ is the spectral distribution of the incident light and $L(\theta_i)$ is a geometrical term of incident light onto the object surface. The intensity of light reflected by the object surface and coming into the camera can be expressed as the product of $L_i(\theta_i, \lambda)$ and the BSRDF $f_r(\theta_i, \theta_r, \lambda)$. Finally, the pixel intensity I is given by:

$$\begin{aligned}
I(\theta_i, \theta_r) &= \int_{\lambda} s(\lambda) L_i(\theta_i, \lambda) f_r(\theta_i, \theta_r, \lambda) d\lambda \\
&= \int_{\lambda} s(\lambda) c(\lambda) L(\theta_i) \{c_D \cos \theta_i + c_S \delta(\theta_i - \theta_r)\} d\lambda \\
&= L(\theta_i) \cos \theta_i \int_{\lambda} s(\lambda) c(\lambda) c_D(\lambda) d\lambda + L(\theta_i) \delta(\theta_i - \theta_r) c_S \int_{\lambda} s(\lambda) c(\lambda) d\lambda
\end{aligned} \tag{EQ6}$$

where $s(\lambda)$ is the spectral response of a camera.

2.2 Reflectance model with two light sources: the sun and the sky

The reflectance model with a single light source was described in the previous section. In this section, we extend the model for the case of two light sources of different spectral and spatial distributions. In our analysis, these two light sources are the sunlight and the blue skylight.

One significant feature of the skylight is its uniformity over the entire hemisphere. The skylight is highly scattered and it appears to be almost constant. For this reason, the spatial distribution of the skylight L_{sky} appears to be constant. As a result, the intensity of incident light (EQ5) in the case of the sunlight and the skylight is represented as:

$$L_i(\theta_i, \lambda) = c_{sun}(\lambda) L_{sun}(\theta_i) + c_{sky}(\lambda) L_{sky} \tag{EQ7}$$

On the other hand, the sunlight is almost a point light source. However, it has a finite size, so we use a narrow Gaussian distribution (Figure 2) to model the sunlight spatial distribution. The center of the distribution is the sun's direction θ_s .

$$L_{sun}(\theta_i - \theta_s) = A \exp\left(\frac{-(\theta_i - \theta_s)^2}{\sigma^2}\right) \tag{EQ8}$$

By incorporating this light model (EQ7) into (EQ6), the pixel intensity is given by:

$$\begin{aligned}
I(\theta_s, \theta_r) = & \int L_{sun}(\theta_i - \theta_s) \cos \theta_i d\theta_i \int s(\lambda) c_{sun}(\lambda) c_D(\lambda) d\lambda \\
& + c_S \int L_{sun}(\theta_i - \theta_s) \delta(\theta_i - \theta_r) d\theta_i \int s(\lambda) c_{sun}(\lambda) d\lambda \\
& + L_{sky} \int \cos \theta_i d\theta_i \int s(\lambda) c_{sky}(\lambda) c_D(\lambda) d\lambda \\
& + L_{sky} c_S \int \delta(\theta_i - \theta_r) d\theta_i \int s(\lambda) c_{sky}(\lambda) d\lambda
\end{aligned} \tag{EQ9}$$

Unfortunately, $\int L_{sun}(\theta_i - \theta_s) \cos \theta_i d\theta_i$ in the first term of the right side of (EQ9) is difficult to evaluate analytically. However, we found that a cosine curve could be a good numerical approximation of the integral as shown in Figure 3. Other terms are simplified further. We finally get the pixel intensity as:

$$I(\theta_s, \theta_r) = K_{sunD} \cos \theta_s + K_{sunS} L_{sun}(\theta_r - \theta_s) + K_{sky} \tag{EQ10}$$

where

$$\begin{aligned}
K_{sunD} &= B \int s(\lambda) c_{sun}(\lambda) c_D(\lambda) d\lambda \\
K_{sunS} &= c_S \int s(\lambda) c_{sun}(\lambda) d\lambda \\
K_{sky} &= L_{sky} \left\{ \int s(\lambda) c_{sky}(\lambda) c_D(\lambda) d\lambda + \int s(\lambda) c_{sun}(\lambda) d\lambda \right\}
\end{aligned} \tag{EQ11}$$

It is important to see that the two reflection components from the skylight is constant with respect to the direction of the sun θ_s and the viewing direction θ_r . B is a scaling factor due to the approximation of the geometry term of the sunlight diffuse reflection by a cosine function. Changing the coordinate system into the viewer-centered coordinate system illustrated in Figure 4, (EQ11) becomes

$$I(\theta_s) = K_{sunD} \cos(\theta_s - \theta_n) + K_{sunS} L_{sun}(2\theta_n - \theta_s) + K_{sky} \tag{EQ12}$$

In our analysis, the reflectance model represented as (EQ12) is used to remove the specular reflection component and for the shape recovery. Separation of the specular reflection component and the diffuse reflection component will be discussed in the section 3. Shape recovery under sunlight will be explained in the section 5.

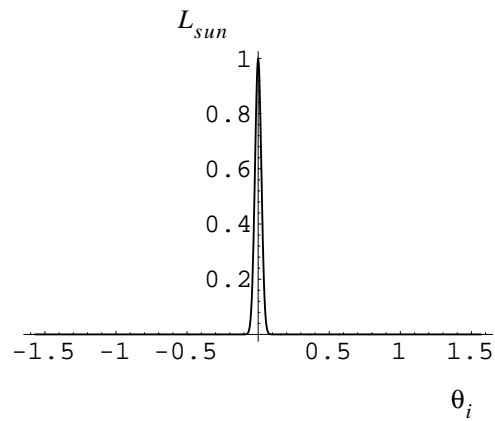


Figure 2 The distribution of the sunlight ($\theta_s = 0$, $\sigma = 0.01\pi$)

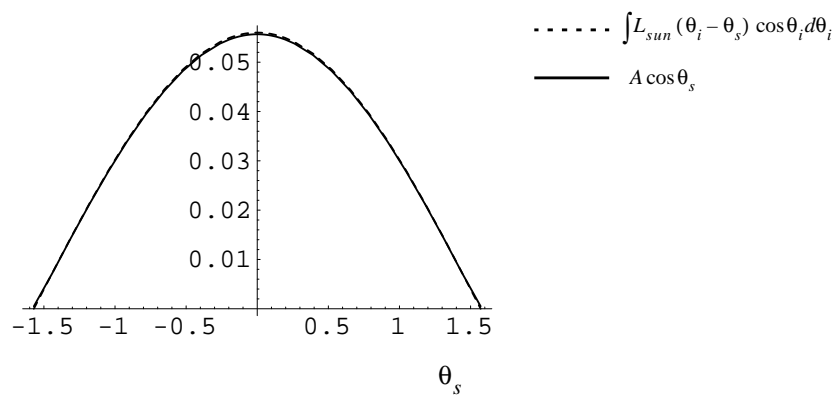


Figure 3 The diffuse reflection of the sun and a cosine curve

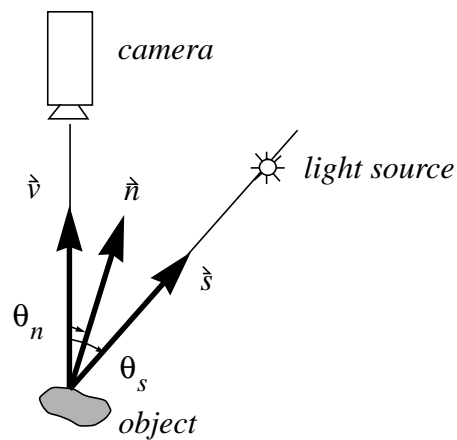


Figure 4 The viewer-centered coordinate system

3 The specular reflection component removal from a sequence of color images

The algorithm to remove the specular reflection component from the sunlight is described in this section. The input to the algorithm is a sequence of outdoor color images taken at different times (i.e. every 15 minutes) on the same day.

3.1 Estimation of the reflection component from the skylight

As stated in the section 2.2, the diffuse and specular reflection components from skylight are constant with respect to the sun direction θ_s and the surface normal direction θ_n . Therefore, shadow regions from the sunlight have uniform pixel intensities since they are illuminated only by the skylight. Pixel intensities in those regions don't have the reflection components from the sunlight. They only have the reflection components from the skylight K_{sky} . For this reason, the value of the reflection component due to the skylight K_{sky} can be obtained as an average pixel intensity in the shadow regions of constant pixel intensity as shown in Color Figure 6. K_{sky} is subtracted from all pixel intensities of the image to yield

$$I(\theta_s) = K_{sunD} \cos(\theta_s - \theta_n) + K_{sunS} L_{sun}(2\theta_n - \theta_s) \quad (\text{EQ13})$$

Then, the pixel intensity has only the diffuse and specular reflection components from sunlight.

3.2 Separation of the two reflection component from the sunlight

The algorithm to separate the two reflection components from the sunlight is described here. The algorithm was originally introduced by Sato and Ikeuchi in [12].

Using red, green, and blue filters, the coefficients K_{sunD} and K_{sunS} , in (EQ13), become two linearly independent vectors, \underline{K}_{sunD} and \underline{K}_{sunS} , unless the colors of the two reflection components are accidentally the same:

$$\underline{K}_{sunD} = \begin{bmatrix} k_{sunDR} \\ k_{sunDG} \\ k_{sunDB} \end{bmatrix} = \begin{bmatrix} \int_{\lambda} \tau_R(\lambda) s(\lambda) c_{sun}(\lambda) c_D(\lambda) d\lambda \\ \int_{\lambda} \tau_G(\lambda) s(\lambda) c_{sun}(\lambda) c_D(\lambda) d\lambda \\ \int_{\lambda} \tau_B(\lambda) s(\lambda) c_{sun}(\lambda) c_D(\lambda) d\lambda \end{bmatrix} \quad (\text{EQ14})$$

$$\underline{K}_{sunS} = \begin{bmatrix} k_{sunSR} \\ k_{sunSG} \\ k_{sunSB} \end{bmatrix} = \begin{bmatrix} c_S \int_{\lambda} \tau_R(\lambda) s(\lambda) c_{sun}(\lambda) d\lambda \\ c_S \int_{\lambda} \tau_G(\lambda) s(\lambda) c_{sun}(\lambda) d\lambda \\ c_S \int_{\lambda} \tau_B(\lambda) s(\lambda) c_{sun}(\lambda) d\lambda \end{bmatrix} \quad (\text{EQ15})$$

These two vectors represent the colors of the diffuse and specular reflection components in the dichromatic reflectance model [13].

First, the pixel intensities in the R, G, and B channels with m different light source directions, are measured at one pixel. It is important to note that all intensities are measured *at the same pixel*. The three sequences of intensity values are stored in the columns of an $m \times 3$ matrix M . Considering the hybrid reflectance model and two color vectors in (EQ13), (EQ14), and (EQ15), the intensity values in the R, G, and B channels can be represented as:

$$\begin{aligned} M &= \begin{bmatrix} \underline{M}_R & \underline{M}_G & \underline{M}_B \end{bmatrix} \\ &= \begin{bmatrix} \cos(\theta_{s1} - \theta_n) & L_{sun}(\theta_{s1} - 2\theta_n) \\ \cos(\theta_{s2} - \theta_n) & L_{sun}(\theta_{s2} - 2\theta_n) \\ \vdots & \vdots \\ \cos(\theta_{sm} - \theta_n) & L_{sun}(\theta_{sm} - 2\theta_n) \end{bmatrix} \begin{bmatrix} k_{sunDR} & k_{sunDG} & k_{sunDB} \\ k_{sunSR} & k_{sunSG} & k_{sunSB} \end{bmatrix} \\ &= \begin{bmatrix} \underline{G}_{sunD} & \underline{G}_{sunS} \end{bmatrix} \begin{bmatrix} \underline{K}_{sunD}^T \\ \underline{K}_{sunS}^T \end{bmatrix} \\ &\equiv GK \end{aligned} \quad (\text{EQ16})$$

where the two vectors \underline{G}_{sunD} and \underline{G}_{sunS} represent the intensity values of the diffuse and specular reflection components with respect to the direction of the sun θ_s . Vector \underline{K}_{sunD} represents the diffuse reflection color vector. Vector \underline{K}_{sunS} represents the specular reflection color vector. We call the two matrices G and K , the *geometry matrix* and the *color matrix*, respectively.

Suppose we have an estimation of the color matrix K . Then, the two reflection components represented by the geometry matrix G are obtained by projecting the observed reflection stored in M onto the two color vectors \underline{K}_{sunD} and \underline{K}_{sunS} .

$$G = MK^+ \quad (\text{EQ17})$$

where K^+ is a 3×2 pseudoinverse matrix of the color matrix K .

The derivation shown above is based on the assumption that the color matrix K is known. The method to estimate the color matrix K , more specifically the two color vectors \underline{K}_{sunD} and \underline{K}_{sunS} , is discussed in the following sections.

3.2.1 Estimation of the illuminant color

Several algorithms have been proposed to estimate illuminant color. The method used by Lee [7] is briefly described here. According to the dichromatic reflectance model [13], the color of reflection from a dielectric object is a linear combination of the diffuse reflection component and the specular reflection component. The color of the specular reflection component is equal to the illuminant color (EQ15). In the x-y chromaticity diagram, the observed color of the dielectric object lies on a segment whose endpoints represent the colors of the diffuse and specular reflection components. By representing the color of each object as a segment in the chromaticity diagram, the illuminant color can then be determined from the intersection of the two segments attributed to the two objects of interest [6].

In our experiment, the row \underline{K}_{sunS}^T of the color matrix, K , which represents illumination color, is estimated by using a method similar to the method described above. First, several pixels of different colors in the image are manually selected (Color Figure 1). The observed reflection color from those selected pixels is a linear combination of the diffuse reflection component and the specular reflection component. By plotting the observed reflection color of each pixel in the x-y chromaticity diagram over the image sequence, we obtain several line segments in the x-y chromaticity dia-

gram. The illuminant color can then be determined by the intersection of those line segments in the diagram. This is shown in Figure 6 for the case of the real image shown in Color Figure 1.

This technique is limited to the case that there are objects of different colors in the image. In other words, if the image contains objects of only one color, the light source color cannot be estimated. In those cases, the illumination color is obtained by measuring the color vector of the light source directly. In our experiment for outdoor color images which will be shown in the section 7, the illumination color of the sunlight is directly measured by using a standard color chart.

3.2.2 Estimation of the diffuse reflection color

The other row \underline{K}_{sunD}^T of the color matrix cannot be obtained in the same manner because it depends on the material of the object. Fortunately, in order to solve this problem, we can use the fact that the distribution of the specular reflection component for the extended light source is limited to a fixed angle, depending on σ in (EQ8). Therefore, if two vectors, $\underline{w}_i = [I_{Ri} \ I_{Gi} \ I_{Bi}]^T$ ($i = 1, 2$) are sampled on the θ_s axis at large enough interval, at least one of these vectors will be equal to the color vector of the diffuse reflection component \underline{K}_{sunD}^T . This vector has no specular reflection component. The desired color vector of the diffuse reflection component \underline{K}_{sunD}^T is the vector \underline{w}_i which subtends the largest angle with respect to the vector \underline{K}_{sunS}^T . The angle between the two color vectors can be calculated as:

$$\beta = \arccos \frac{\underline{K}_{sunS}^T \cdot \underline{w}_i}{|\underline{K}_{sunS}^T| |\underline{w}_i|} \quad (\text{EQ18})$$

Once we get the color matrix K , the geometry matrix G can be calculated from (EQ17).

$$M_{diffuse} = \underline{G}_D \underline{K}_D^T \quad (\text{EQ19})$$

$$M_{surface} = \underline{G}_S \underline{K}_S^T \quad (\text{EQ20})$$

After the reflection components from the skylight and the specular reflection component from the sunlight are removed by the method explained in the section 3, the pixel intensities in the image are modeled by the equation:

$$\begin{bmatrix} I_R(\theta_s) \\ I_G(\theta_s) \\ I_B(\theta_s) \end{bmatrix} = \begin{bmatrix} K_{sunDR} \\ K_{sunDG} \\ K_{sunDB} \end{bmatrix} \cos(\theta_s - \theta_n) \quad \text{(EQ21)}$$

Since the pixel intensity now has only the diffuse reflection component from the sunlight, the intensities in three color bands are redundant for the purpose of shape recovery. Thus, only one band of the three color bands is used in our discussions on surface albedo normalization and surface normal determination.

$$I(\theta_s) = K_{sunD} \cos(\theta_s - \theta_n) \quad \text{(EQ22)}$$

4 The normalization of surface albedo K_{sunD}

In this section, the method to normalize the surface albedo K_{sunD} is discussed. The shape recovery algorithm will be explained in the section 5. The object image with non-uniform surface albedo (Color Figure 2) is normalized to yield the image of the object with uniform surface albedo (Figure 8).

The object in the image may not have a uniform surface albedo, i.e. several regions of different colors may be on the object surface. If this is the case, the shape recovery method based on the assumption of a uniform surface albedo will fail. Therefore, we need to apply a method to normalize the surface albedo to obtain an image for shape recovery as if the object had a surface with a uniform surface albedo K_{sunD} .

Recently, Nayar and Bolle [9] proposed to use a ratio of surface albedos of neighboring uniform surface albedo regions for object recognition purposes. A similar technique is used for our analysis, in this case, the normalization of the surface albedo. First, the object surface is segmented into regions with uniform albedos divided by a boundary where a pixel intensity changes abruptly. Consider two neighboring pixels at the boundary. One pixel lies in the region A and the other exists in the region B . The two points on the object surface which correspond to the two image pixels are assumed to have the same surface normal, for a smooth continuous surface. In this case, the intensities of the two pixels are given from (EQ22) as:

$$I^A(\theta_s) = K_{sunD}^A \cos(\theta_s - \theta_n) \quad (\text{EQ23})$$

$$I^B(\theta_s) = K_{sunD}^B \cos(\theta_s - \theta_n) \quad (\text{EQ24})$$

As you can see in the equations above, the ratio of the two surface albedos K_{sunD}^A and K_{sunD}^B is equal to the ratio of the two pixel intensities I^A and I^B . This is because the two surface points corresponding to the two image pixels have the same surface normal direction θ_n .

$$\frac{K_{sunD}^A}{K_{sunD}^B} = \frac{I^A}{I^B} \quad (\text{EQ25})$$

This surface albedo ratio is computed at all points along the boundary between the region A and the region B . Then, the surface albedo ratio of the two regions is given as the average of all computed ratios. By repeating the same procedure for all pair of two neighboring regions in the image, we obtain a table of surface albedo ratios. The surface albedo ratios are propagated in the table, so that surface albedo ratio of all pairs of any two regions are obtained unless some regions are completely isolated from others. For instance, consider the two separated regions A and B , and the region C between the two regions. The surface reflectance ratio between the region A and B is computed as:

$$\frac{K_{sunD}^A}{K_{sunD}^B} = \frac{K_{sunD}^A}{K_{sunD}^C} \cdot \frac{K_{sunD}^C}{K_{sunD}^B} \quad (\text{EQ26})$$

The surface albedo ratio can be computed by using another technique. The use of the Land's retinex theory [6] for calculating surface albedo was first introduced by Horn [3]. In this algorithm, the Laplacian operator is first applied to the logarithm of image pixel intensities in order to emphasize edges. The result is thresholded to remove smooth intensity fluctuations due to spatial variations in the incident light distribution. Finally, the logarithm of lightness is estimated by convolving the result with the inverse Laplacian operator. By using the algorithm, Horn successfully obtained the image intensity which is an estimation of the surface albedo. The estimation of surface albedo can be used for normalizing the surface albedo prior to shape recovery in our analysis of outdoor scene. Unfortunately, we found that the algorithm based on the Land's retinex theory is not as robust as the other method described in this section for most images. Therefore, we decided to use the method to measure the surface albedo ratio directly.

5 Obtaining surface normals

5.1 Two sets of surface normals

After the specular reflection removal and the surface albedo normalization, the input image sequence has only the diffuse reflection component from the sunlight. Usually, shape from shading and photometric stereo are used for recovering shape information from diffuse reflection images. Initially, those techniques are implemented for shape recovery in our experiments. However, we unfortunately found that neither of those techniques could yield correct object shapes. It is attributed to various sources of noise in the input image such as incomplete removal of the specular reflection component. Shape from shading and photometric stereo use very small number of images for surface normal computation. That leads us to an erroneous object shape when the images contain slight errors in pixel intensities. Therefore, we decided to use another algorithm to determine surface normals from the input image sequence. The algorithm makes use of more images in the sequence, rather than just few of them. We describe the algorithm in this section.

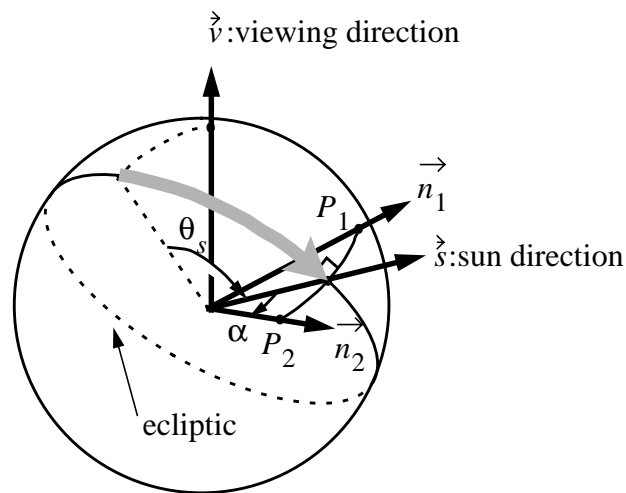


Figure 5 Sun direction, viewing direction and surface normal in 3D case

To represent the sun's motion in three dimensional space, we consider the Gaussian sphere as shown in Figure 5. The ecliptic is represented as the great circle on the Gaussian sphere. The viewing direction \vec{v} is fixed. The direction of the sun \vec{s} is specified as the function of θ_s in the plane of the ecliptic.

Consider an intensity of one pixel as the function of the sun direction $I(\theta_s)$. If the maximum intensity is observed when the sun is located at the direction θ_s' , the surface normal of the image pixel should be located somewhere on the great circle P_1P_2 which is perpendicular to the ecliptic. For obtaining robust estimations, the maximum pixel intensity I' and the direction of the sun θ_s' are found by fitting a second degree polynomial to the observed pixel intensity sequence. According to the reflectance model (EQ22), the angle between the sun direction \hat{s} and the surface normal directions \vec{n}_1 and \vec{n}_2 on the great circle P_1P_2 is given by:

$$\alpha = \text{acos}\left(\frac{I'}{K_{sunD}}\right) \quad (\text{EQ27})$$

The surface albedo K_{sunD} has to be known for computing α . If we assume that at least one surface normal on the object surface is the same as the sun direction \hat{s} , the surface albedo K_{sunD} is simply obtained as the intensity of the pixel $I = K_{sunD}$. The pixel in the image can be found simply as the brightest pixel. In a practical case, the estimation of the surface albedo is computed as the average of the brightest pixel intensities from multiple images of the input image sequence, for robustness. We empirically found the algorithm described in this section works better for estimating surface normals in our analysis.

5.2 Unique surface normal solution

Due to the sun's restricted movement on the ecliptic, we cannot obtain a unique solution for surface normal by applying photometric stereo to outdoor images taken at different times at the same day. This fact was pointed out by Woodham [15] when he introduced the photometric stereo method. As a result, there has been no attempts reported for recovering an object shape by the photometric stereo method applied to outdoor images. However, Onn and Bruckstein [11] recently studied photometric stereo applied to two images and showed that surface normals can be determined uniquely even if only two images are used, except some special cases.

By using the algorithm described in the previous section, two sets of surface normals \vec{n}_1 and \vec{n}_2 are obtained. We used the constraint which Onn called integrability constraint, in order to choose a correct set of surface normals out of the two sets of surface normals.

$$\begin{aligned}\vec{n}_1 &= (-p_1, -q_1, 1) \\ \vec{n}_2 &= (-p_2, -q_2, 1)\end{aligned}\tag{EQ28}$$

The Onn's integrability constraint is described briefly here. First, we compute two surface normals \vec{n}_1 and \vec{n}_2 for all pixels. Then, the object surface is segmented into subregions by defining a boundary where two surface normals are similar. In practice, if an angle between \vec{n}_1 and \vec{n}_2 is within a threshold, the pixel is included in the boundary. Then, for each subregion R , two integrals are computed.

$$\int_{(x,y) \in R} \left(\frac{\partial p_1}{\partial y} - \frac{\partial q_1}{\partial x} \right)^2 dx dy\tag{EQ29}$$

$$\int_{(x,y) \in R} \left(\frac{\partial p_2}{\partial y} - \frac{\partial q_2}{\partial x} \right)^2 dx dy\tag{EQ30}$$

Theoretically, the correct set of surface normals produces the integral value equal to zero. In a practical case, the correct surface normal set can be chosen as the one with the integral value close to zero. Onn and Bruckstein showed that the integrability constraint is always valid except for a few rare cases where the object surface can be represented as $H(x, y) = F(x) + G(y)$ in a suitably defined coordinate system. In our experiments, the exceptional case does not occur, so the integrability constraint can be used for obtaining a unique solution for surface normals.

6 Experimental results: laboratory setup

In the previous sections, we described the three algorithms which are essential for analyzing real color images taken under the sun. They include 1. the separation of the reflection components from the two light sources: the sunlight and the skylight, 2. the normalization of the surface albedo and 3. the unique solution for surface normals. In this section, we applied the algorithms for color image sequences taken in a laboratory setup, in order to demonstrate the feasibility of the algorithms. A SONY CCD color video camera module model XC-711 is used to take all images. In our experimental setup, the object is placed at the center of the origin of the world coordinate system, and the color video camera is placed at the top of the object. The sunlight is simulated by a small halogen lamp attached to a PUMA 560 manipulator which moves around the object on its equatorial plane. The skylight is not simulated in our experimental setup. The effect of the skylight and separation of the reflection components from the skylight will be described in the section 7.

6.1 The specular reflection color estimation

The algorithms to estimate the illumination color, and consequently, to separate multiple reflection components are applied to a real color image sequence. A shiny ceramic brooch which is painted in several colors is used in this experiment. First, a sequence of color images was taken as the point light source was moved around the object from $\theta_s = -50^\circ$ to $\theta_s = 50$ by the step of 10° . As described in the section 3.2.1, three pixels of different colors in the image are manually selected. The 6th frame of the color image sequence and the manually selected pixels are shown in Color Figure 1. The observed reflection color of each pixel is plotted in the x-y chromaticity diagram over the image sequence to obtain a line segment in the x-y chromaticity diagram (Figure 6). Then, the illuminant color which is equal to the specular reflection color \underline{K}_{sunS} can then be determined by the intersection of the three line segments. In this experiment, the specular reflection color vector was estimated as $\underline{K}_{sunS}^T = (0.353, 0.334, 0.313)$.

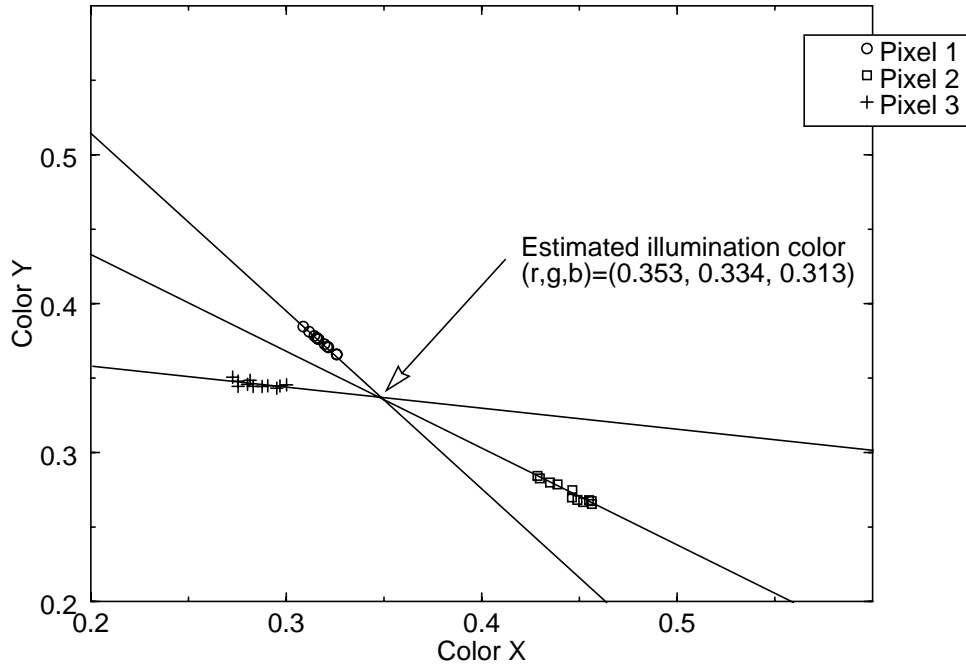


Figure 6 Estimation of illuminant color in the x-y chromaticity diagram
Those three pixels of different colors are manually selected in the image (Color Figure 1).

6.2 The specular reflection component removal

The algorithm for separating the specular reflection component and the diffuse reflection component from the sunlight, described in the section 3.2, is applied to the input color image sequence. As stated in the section 3.2, the algorithm is applied at each pixel basis. For each pixel in the image, the red, green and blue intensities over the image sequence are initially stored in the matrix M as its columns. With the estimated specular reflection color vector \tilde{K}_{sunS} from the previous section, the diffuse reflection color vector \tilde{K}_{sunD} for the pixel is estimated by the algorithm explained in the section 3.2.2. Then, by using the estimations of the two reflection color vectors, the geometry matrix G is obtained from (EQ17). Finally, the two reflection components which are observed at the pixel over the image sequence are separated by using (EQ19) and (EQ20).

By using the pixel-based separation algorithm, we can generate two images of the two reflection components. The algorithm is applied to all pixels of the input color image separately, and each separated reflection component was used to generate the diffuse reflection component image sequence and the specular reflection component image sequence. The 6th frames of the diffuse reflection component image sequence and the specular reflection component image sequence are

shown in Color Figure 2 and Color Figure 3, respectively.

6.3 Albedo normalization

After the specular reflection component from the sunlight is removed from the color image sequence, we obtain the color image sequence which includes only the diffuse reflection component from the sunlight. The algorithm to normalize the surface albedo on the object surface, described in the section 4 is applied to the resulting image sequence. Note that only one color band (for examples, in our case, the red band) is used for the normalization of the surface albedo and the shape recovery. This is because intensity profiles of all of the three color bands are equivalent in terms of shape recovery when the images include only the diffuse reflection component. Therefore, those three color bands are redundant, and using only one band is sufficient.

The 6th frame of the diffuse reflection image sequence which is shown in Color Figure 2 is used here. First, by detecting boundary edges, the object surface is segmented into subregions, each of which has a uniform surface albedo. The boundary edges are defined as a group of pixels where pixel intensities change abruptly. On the other hand, pixel intensities change gradually within each of the subregions. After the segmentation of the object surface, all regions are uniquely labeled by using the sequential labeling algorithm. The result of the region segmentation and the sequential labeling is shown in Figure 7.

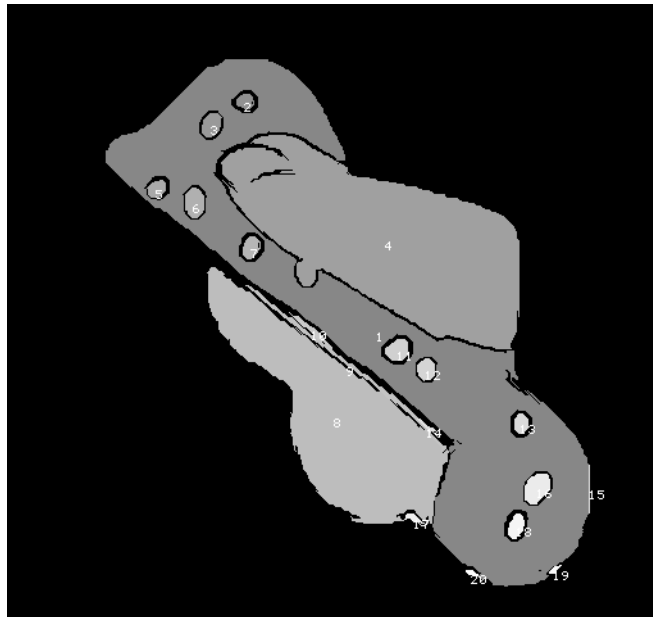


Figure 7 Segmented uniform albedo regions

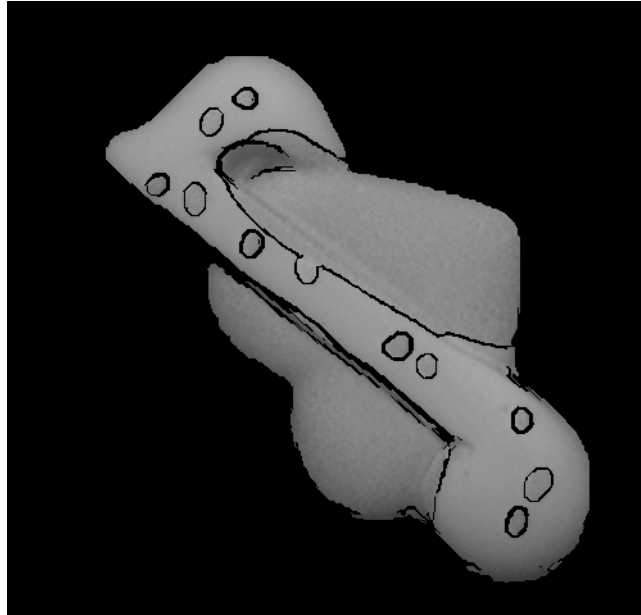


Figure 8 The frame 6 with normalized albedo in red band

Then, surface albedo ratios between all pairs of two neighboring subregions are computed. Consider that we compute the surface albedo ratio between the region A and the region B . For each pixel of the region A which exists at the boundary between the two regions, the pixel of the region B which is closest to the pixel in the region A is selected. Then, the ratio of the two pixel intensities is used as the surface reflectance ratio (EQ25) between the region A and the region B . In order to obtain a more accurate estimation of the ratio, all pixels along the boundary are used to compute the average of the ratio. The average ratio is used as the surface ratio between the region A and the region B . The same procedure is repeated for all pairs of two neighboring regions to build a table of the surface albedo ratio. Then, the surface albedo ratios are propagated in the table, so that the surface albedo ratios of all pairs of any two non-isolated regions are obtained. Finally, the computed surface albedo ratios are used for normalizing image intensities of all frames in the image sequence. Figure 8 shows the normalization result. All pixel intensities of the object surface are normalized as if the object had a uniform surface albedo corresponding to the region 1 in Figure 7. This normalized diffuse reflection image is used for recovering the object shape.

6.4 Unique solution for surface normal

In this section, the algorithm to determine surface normals uniquely, which was described in the

section 5, is applied to a sequence of real color images taken in our laboratory setup. A plastic dinosaur face is used for this experiment. The sequence of color images was taken as the point light source was moved around the object from $\theta_s = -70^\circ$ to $\theta_s = 70^\circ$ by the step of 5° . The specular reflection component is removed from the input image sequence by using the same algorithm used in the section 6.2. In this experiment, the specular reflection color was directly measured rather than estimating as described in the section 6.1. The 8th frame of the resulting diffuse reflection image sequence is shown in Color Figure 4.

The algorithm for obtaining two sets of surface normals which was described in the section 5.1 was applied to the red band of the resulting diffuse reflection image sequence. Computed two sets of surface normals \vec{n}_1 and \vec{n}_2 are shown in Figure 9 as a needle diagram. Subsequently, the integrability constraint was applied to determine the correct set of surface normals uniquely. First, the object surface was segmented into subregions by defining a boundary where the two surface normals \vec{n}_1 and \vec{n}_2 are similar. The obtained boundary is shown in Figure 10. Theoretically, the boundary should be connected and narrow. However, in a practical case, the obtained boundary tends to be wide in order to guarantee its connectivity. Thus, the thinning operation, in our case the medial axis transformation, was applied to narrow the boundary. Figure 11 shows the resulting boundary after the medial axis transformation.

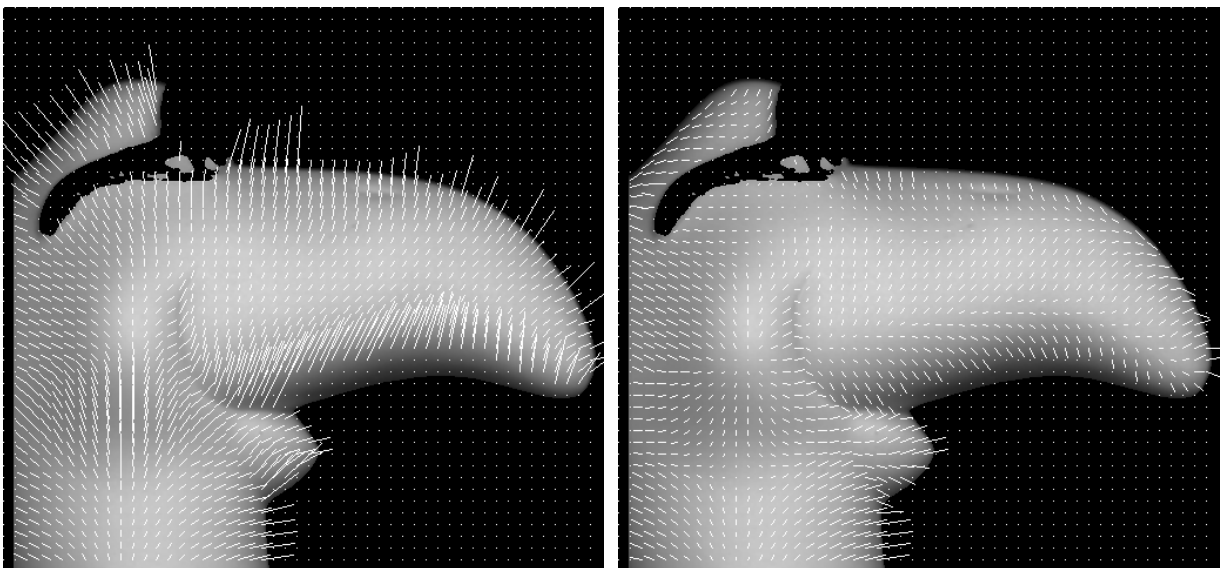


Figure 9 Two sets of surface normals

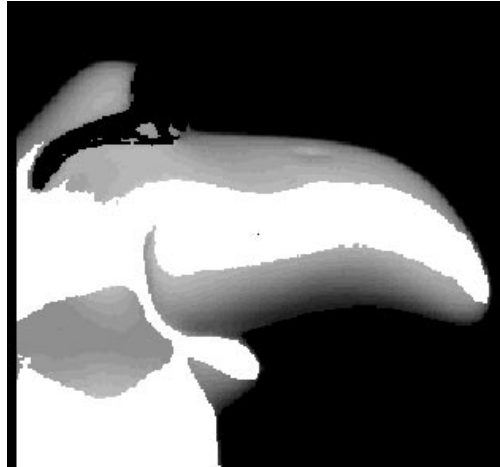


Figure 10 The boundary region obtained from two surface normal sets

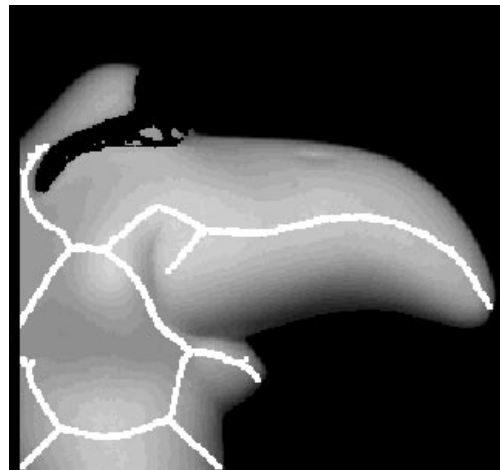


Figure 11 The boundary after medial axis transformation

Then, a standard sequential labeling algorithm was applied to the segmented regions to assign unique labels as illustrated in Figure 12. In the figure, the labels are represented by different gray levels. Finally, the integrability constraint is applied to obtain the correct set of surface normals in each labeled region as explained in the section 5.2. The unique surface normal solution is shown in Figure 13. Finally, the object surface shape was recovered by using a standard height from normals procedure. In our implementation, the relaxation method proposed by Horn and Brooks [5] was used. Figure 14 shows the surface shape of the dinosaur's face.

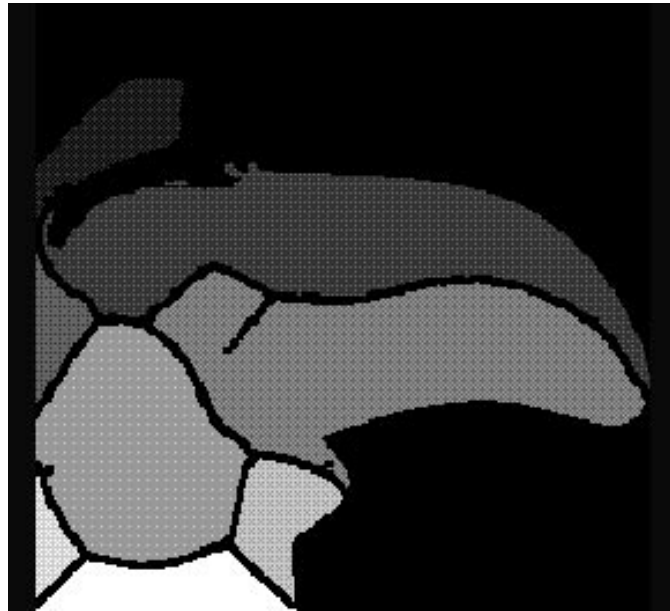


Figure 12 Segmented regions (gray levels represent regions)

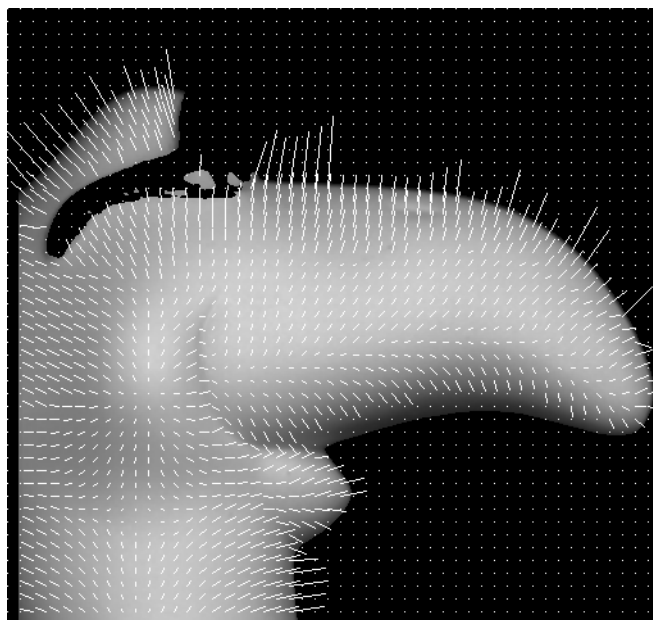


Figure 13 Right surface normal set

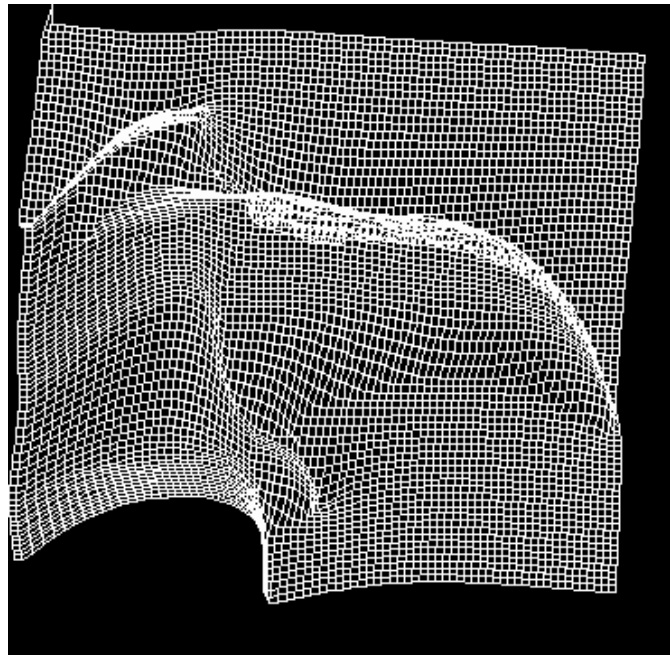


Figure 14 Recovered object shape

7 Experimental result: outdoor scene (water tower)

In this section, we demonstrate successful reflection component separation and shape recovery under solar illumination. To this end, the algorithms described in this paper were applied to real images of a water tower (Color Figure 5) taken in an outdoor environment under the sun. A clear day was chosen for taking the images in Pittsburgh, PA to avoid the undesirable effects of clouds in the sky. A SONY CCD color video camera modules model XC-711 was used to take all images, and the images are recorded by using a U-matic video recorder. Later, the images are digitized from the recorded U-matic tape every fifteen minutes. The first image frame was taken at 10:45am, and the last frame was taken at 4:15pm. In this manner, we took 23 frames of color images in total. As an example, the image frame taken at 2:15pm is shown in Color Figure 5.

First, the region of interest corresponding to the water tower was extracted. The skylight is almost uniform through a day from the sunrise until the sunset. As a result, all background pixels which corresponds to the sky can be defined as pixels with low intensity variation. At each pixel in the image, the variance of the pixel intensity over the time sequence is computed. Then, all pixels with little intensity variation are removed by applying a simple threshold, in order to extract the region of interest for the further processing. The extracted region of interest is shown in Color Figure 6.

The next step is to remove the reflection component from the skylight. According to the reflection model under the solar illumination (EQ12) that we developed in the section 2.2, the two reflection components due to the skylight are represented as a constant value K_{sky} . The constant value K_{sky} can be estimated as an average pixel color of a uniform intensity region which is in a shadow from the sunlight. In our experiment, the region of a constant pixel colors is selected manually as shown in Color Figure 6. The measured pixel color within the region is $(r, g, b) = (14.8, 17.2, 19.5)$ with the variance $(0.2, 0.3, 0.6)$. The pixel color vector was subtracted from intensities of all pixels to eliminate effects from the skylight. After this operation, the color images have only the reflection components due to the sunlight. The resulting image is shown in Color Figure 7. It can be seen that the image has more contrast between an illuminated region and a shadow region, compared to the image with the reflection component due to the skylight (Color Figure 6). All of frames of the input color images are processed in the same manner

to remove the reflection component due to the skylight.

After the removal of the reflection component from the skylight, the sequence of color images includes two reflection component: the diffuse reflection component and the specular reflection component due to the sunlight as modeled by (EQ13). The algorithm to remove the specular reflection component explained in the section 3.2 was applied to the resulting color images. At each pixel in the color image, the two reflection components were separated and only the diffuse reflection component was used for further shape recovery. As an example, one frame of the resulting color image sequence is shown in Color Figure 8. The image includes only one reflection component: the diffuse reflection component from the sunlight. The water tower appears to have a uniform surface albedo. Therefore, it was not necessary to apply the surface albedo normalization procedure explained in the section 4 in this experiment.

The algorithm to determine surface normals uniquely by using an image sequence was applied to the red band of the resulting color image sequence. Figure 15 shows the recovered surface normals of the water tower. Note that surface normals are not obtained in the lower right part of the water tower. This is because, in the region, the maximum intensity is not observed at each pixel through the image sequence. To recover surface normals in the region, we need to take an input image sequence over a longer period of time than this experiment. Also, another techniques such as photometric stereo can be used for recovering surface normals in the region. However, in this case, it will be hard to estimate surface normals accurately. Finally, the relaxation method for calculating height from surface normals was applied. The recovered shape of the part of the water tower is shown in Figure 16.

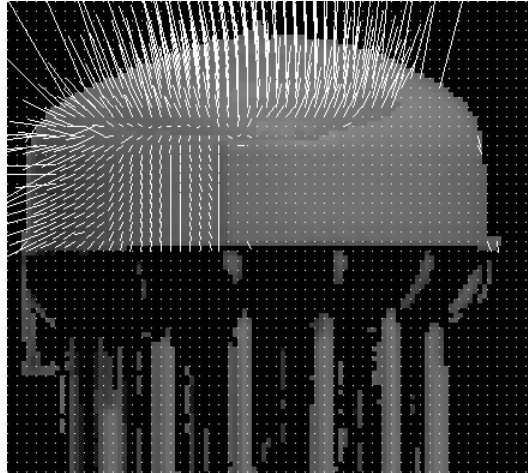


Figure 15 Surface normals

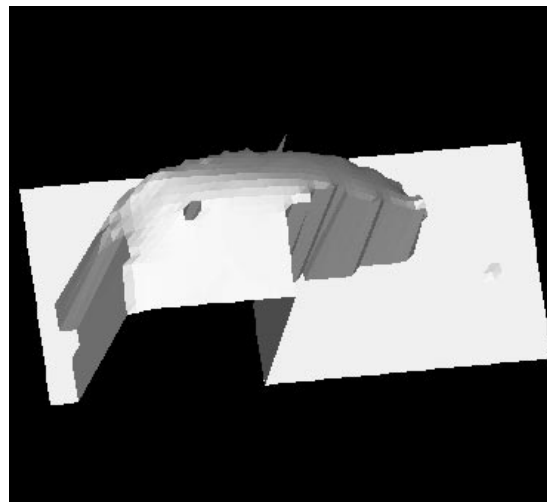
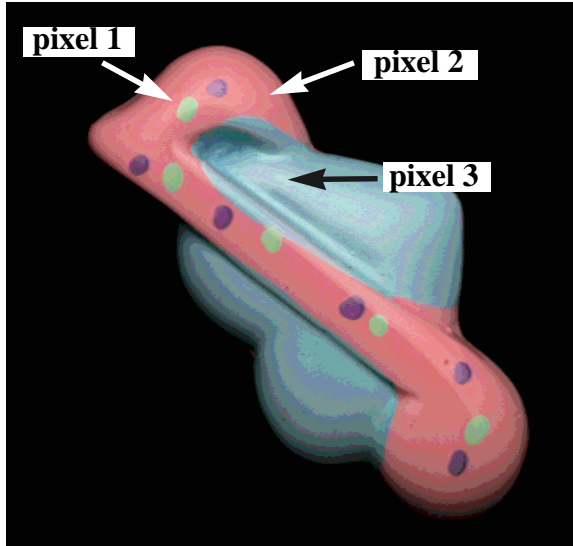


Figure 16 Recovered shape of the water tank

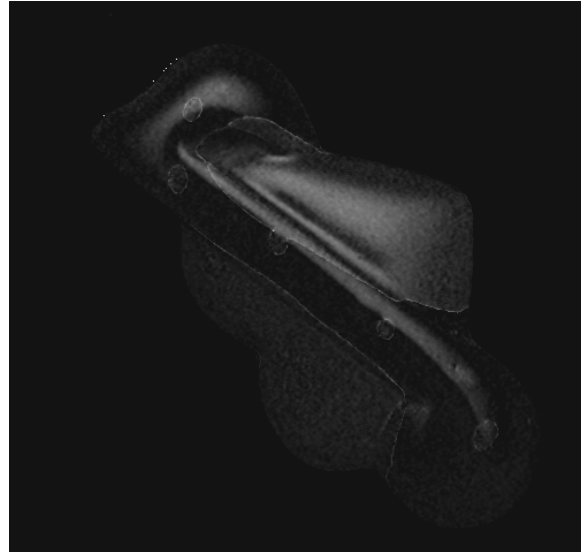
8 Conclusions

We studied image analysis of an outdoor scene in this paper. The scope of traditional techniques for reflectance analysis such as shape from shading and photometric stereo has been highly restricted to images taken under a controlled laboratory setup. It is attributed to the fundamental difficulties in analyzing real images taken in an outdoor environment. First, we addressed the difficulties involved in analyzing real outdoor images under the solar illumination. They include 1. multiple reflection components due to multiple light sources of different spectral and spatial distribution, namely the sunlight and the skylight, 2. non-uniform surface albedos and 3. ambiguity in surface normal determination caused by the sun's restricted motion. For each of those three problems, solutions were proposed based on the reflectance model under the solar illumination which we developed. Finally, the effectiveness of the algorithms were successfully demonstrated by using real color images taken both in a laboratory setup simulating the sunlight and in an outdoor environment. We believe this is one of the first attempts for analyzing reflection on object surfaces in an outdoor scene.

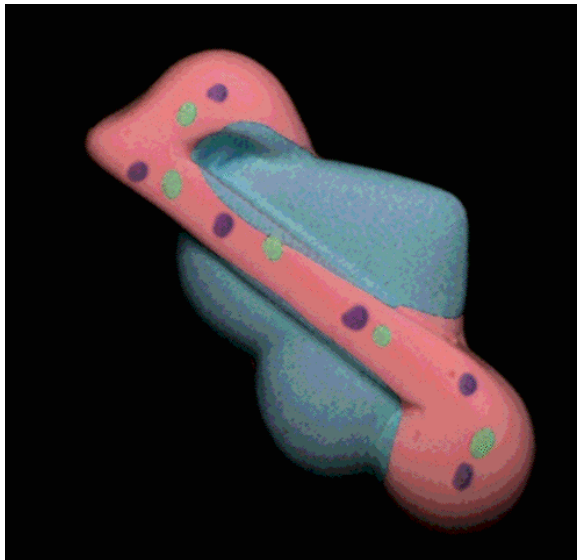
Color figures



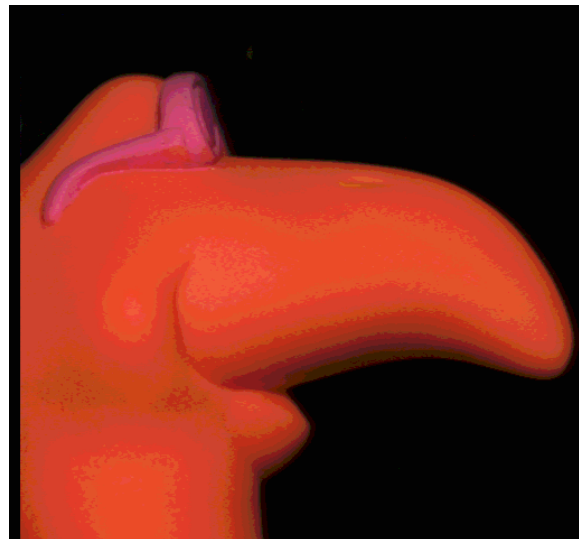
Color Figure 1 Input color image sequence (frame 6 is shown) and manually selected pixels



Color Figure 3 specular reflection component of the frame 6



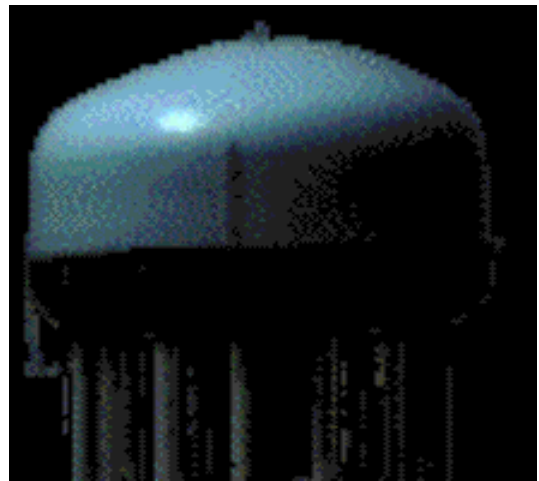
Color Figure 2 Diffuse reflection component of the frame 6



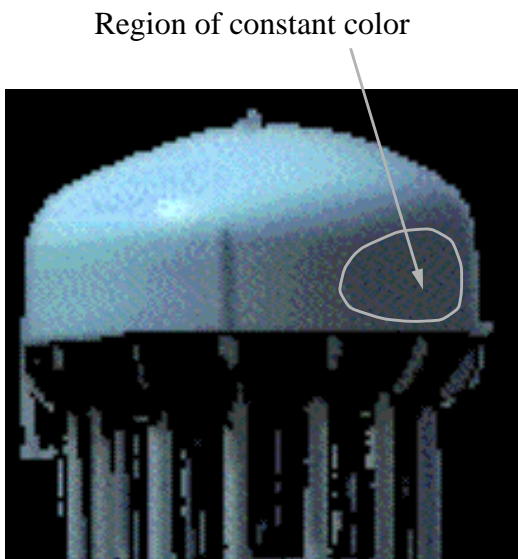
Color Figure 4 Diffuse reflection component image (frame 8)



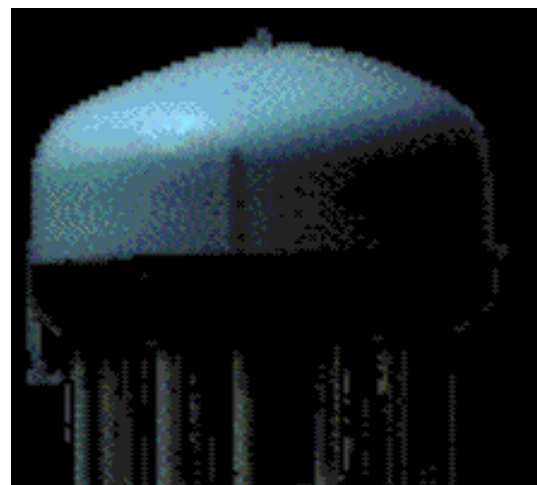
Color Figure 5 Outdoor intensity image (water tank frame 15)



Color Figure 7 Water tank image without sky reflection component



Color Figure 6 Extracted region of interest



Color Figure 8 Water tank image after highlight removal

Acknowledgments

The authors are thankful to Fred Solomon for his valuable comments on the manuscript.

References

- [1] P. Beckmann and A. Spizzichino, *The scattering of electromagnetic waves from rough surfaces*, Pergamon Press, 1963.
- [2] G. E. Healey, S. A. Shafer and L. B. Wolff (eds.), *Color (physics-based vision)*, Jones and Bartlett, Boston, 1992.
- [3] B. K. P. Horn, "Determining lightness from an image," *Computer Graphics and Image Processing*, Vol. 3, No. 1, pp. 277-299, December 1974.
- [4] B. K. P. Horn, "Obtaining shape from shading information," in B. K. P. Horn and M. J. Brooks (Ed.), *Shape from Shading*, MIT Press, pp. 123-171, Cambridge, 1989.
- [5] B. K. P. Horn and M. J. Brooks, "The variational approach to shape from shading," *Computer Vision, Graphics Image Processing*, Vol. 33, pp. 174-203, 1986.
- [6] E. H. Land, "The retinex," *American Scientist*, Vol. 52, No. 2, pp. 247-264, June 1964.
- [7] H. C. Lee, "Method for computing the scene-illuminant chromaticity from specular highlights," *J. Opt. Soc. Am. A*, Vol. 3, No. 10, pp. 1694-1699, 1986.
- [8] H. C. Lee, E. J. Breneman, and C. P. Schulte, "Modeling light reflection for computer color vision," *IEEE Transactions on Pattern Analysis and Machine Intelligence*, Vol. 12, No. 4, pp. 402-409, April 1990.
- [9] S. K. Nayar and R. M. Bolle, "Object recognition based on reflectance and geometry," *Proceedings of the SPIE*, vol. 2031, pp. 328-42, July 1993.
- [10] S. K. Nayar, K. Ikeuchi, and T. Kanade, "Determining shape and reflectance of hybrid surfaces by photometric sampling," *IEEE Trans. on Robotics and Automation*, Vol. 6, No. 4, pp. 418-431, 1990.
- [11] R. Onn and A. Bruckstein, "Integrability disambiguates surface recovery in two-image photometric stereo," *International Journal of Computer Vision*, Vol. 5, No. 1, pp. 105-113, 1990.
- [12] Y. Sato and K. Ikeuchi, "Temporal-color space analysis of reflection," *Journal of Optical*

Society of America A, Vol. 11, No. 11, pp. 2990-3002, November 1994.

- [13] S. A. Shafer, "Using color to separate reflection components," *COLOR Research and Application*, Vol. 10, No. 4, pp. 210-218, 1985.
- [14] K. Torrance and E. Sparrow, "Theory for off-specular reflection from roughened surfaces," *Journal of the Optical Society of America*, No. 57, pp. 1105 - 1114, 1967.
- [15] R. J. Woodham, "Photometric Stereo: A reflectance map technique for determining surface orientation from image intensity," *Proc. SPIE*, Vol. 155, pp. 136-143, 1978.